Journal Pre-proof

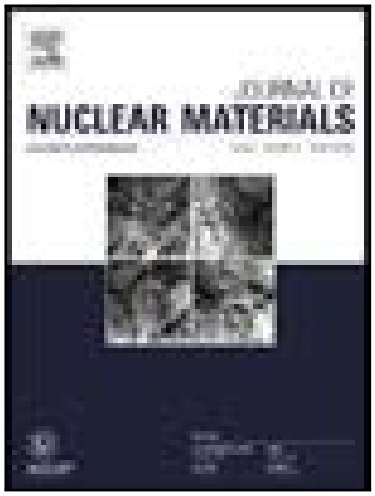

Irradiation-enhanced diffusion and diffusion-limited creep in U_3Si_2

M.W.D. Cooper, K.A. Gamble, L. Capolungo, C. Matthews,
D.A. Andersson, B. Beeler, C.R Stanek, K. Metzger

PII: S0022-3115(21)00352-4
DOI: https://doi.org/10.1016/j.jnucmat.2021.153129
Reference: NUMA 153129

To appear in: *Journal of Nuclear Materials*

Received date: 9 March 2021
Revised date: 7 May 2021
Accepted date: 29 May 2021

Please cite this article as: M.W.D. Cooper, K.A. Gamble, L. Capolungo, C. Matthews, D.A. Andersson, B. Beeler, C.R Stanek, K. Metzger, Irradiation-enhanced diffusion and diffusion-limited creep in U_3Si_2, *Journal of Nuclear Materials* (2021), doi: https://doi.org/10.1016/j.jnucmat.2021.153129

Irradiation-enhanced diffusion and diffusion-limited creep in U_3Si_2

M. W. D. Cooper[a], K. A. Gamble[b], L. Capolungo[a], C. Matthews[a], D. A. Andersson[a], B. Beeler[c], C. R Stanek[a], K. Metzger[d]

[a] *Materials Science and Technology Division, Los Alamos National Laboratory P.O. Box 1663, Los Alamos, NM 87545, USA*
[b] *Idaho National Laboratory, Computational Mechanics and Materials Department, Idaho Falls, ID 83415, USA*
[c] *North Carolina State University, USA*
[d] *Westinghouse Electric Company LLC, 1001 Pinnacle Pointe Drive Columbia, SC 29223*

Abstract

U_3Si_2 is an advanced fuel candidate due to its relatively high fissile density and attractive thermal properties. Compared to standard UO_2 fuel, there are significant data gaps for the thermophysical and thermomechanical properties of U_3Si_2. Point defect concentrations and mobilities under irradiation govern a number of important fuel performance properties, such as creep and fission gas release. In this work, we utilized density functional theory (DFT) data to inform a cluster dynamics framework to predict point defect concentrations in U_3Si_2 under irradiation. Molecular dynamics (MD) simulations were used to examine the contribution of atomic mixing during ballistic cascades to diffusion, as well as the diffusivity of U and Si at grain boundaries. These atomic scale models for diffusivity were then used to inform a creep model based on bulk (Nabarro-Herring) and grain boundary (Coble) diffusional creep, and climb-limited dislocation creep. The model compares well against available experimental data and has been implemented in the BISON fuel performance code. A demonstration case using simple power profiles has been carried out, showing that negligible creep occurs due to the low temperatures experienced by U_3Si_2 in-reactor, a consequence of its high thermal conductivity.

1. Introduction

Nuclear fuel must operate within well-defined criteria under the conditions created within a reactor. During its lifetime, nuclear fuel undergoes significant compositional change as it is exposed to high levels of radiation damage, and experiences an extreme heat flux. The latter, in combination with the poor thermal conductivity of UO_2 (especially at high burnup), creates extreme temperature gradients in standard UO_2 fuel. As such, despite the high melting point of UO_2, there is a large amount of stored energy and the possibility of centerline melting is a concern during accident conditions. Fuels that exhibit higher thermal conductivity benefit from a reduced risk of fuel melting. Typically materials without a bandgap, such as UN [1, 2], U_3Si_2 [3], and UB_2 [4, 5], are suitable due to high electronic heat transfer.

Uranium silicide compounds have been widely used in low temperature research reactors, often as dispersion fuels within an aluminum matrix [6–11]. U_3Si_2 has replaced the more uranium dense U_3Si due to its reduced in-pile swelling [12–19]. More recently, monolithic U_3Si_2 has been considered as an accident tolerant fuel candidate for light water reactors (LWRs) due to its high thermal conductivity [3], while also exhibiting higher uranium density than standard UO_2 fuel.

While these properties highlight the potential benefits of U_3Si_2 as an LWR fuel concept, work must be done to address the reaction of U_3Si_2 with steam [20, 21]. Another important factor for fuel safety is the creep of the pellet, which impacts the stress imparted on the clad by the pellet, as well as the pellet-clad gap, which governs the gap conductance, thereby influencing pellet temperatures. Therefore, understanding the underlying processes mediating creep in advanced fuels, such as U_3Si_2, is critical to understanding the extent of their accident tolerance.

Diffusional creep has two contributions: i) bulk diffusion (Nabarro-Herring creep [22]) and ii) grain boundary diffusion (Coble creep [23]). Both of these processes are driven by the effect of stress on the point defect flux within the medium. Vacancies migrate away from tensile regions towards compressive regions, where the vacancy formation energy is lower. Conversely, interstitials migrate away from compressive regions towards tensile regions, where the interstitial formation energy is lower. In both cases, this results in net self-diffusion from the compressive to the tensile region, leading to diffusional creep. U_3Si_2 creep models have previously been derived from experimental data [24]. An alternative to empirical models is to quantify the equilibrium and non-equilibrium defect concentrations and associated migration barriers in the bulk lattice or in the grain boundaries (e.g. from atomic scale simulations), then parameterize a constitutive model accounting for temperature dependent contributions of both Nabarro-Herring and Coble creep mechanisms. In addition, climb-limited dislocation creep is rate limited by the current of point defects to the dislocation core. Thereby, a detailed study of the thermodynamics and kinetics of points defects has the potential to yield a constitutive model accounting for all three aforementioned diffusion-mediated creep mechanisms.

Atomic scale simulations have proven effective at giving insight into the underlying processes that govern diffusion in UO_2 fuel [25–29]. There are three diffusion regimes for Xe and U in UO_2 under irradiation that we also expect to be important for diffusion in U_3Si_2: i) thermal equilibrium diffusion (D_1), ii) irradiation-enhanced diffusion (D_2), and iii) athermal irradiation-induced diffusion due to atomic mixing during damage events (D_3). Density functional theory (DFT) calculations give a good comparison to experiments on UO_2 for D_1 [25–27]. By using the DFT data from Perriot et al. [27] to parameterize a cluster dynamics model, Matthews et al. were able to simulate the D_2 diffusion regime for Xe diffusion [29] and U self-diffusion in UO_2 [28]. Classical molecular dynamics (MD) simulations of irradiation damage processes have been employed to study the athermal D_3 diffusion regime of self- and Xe diffusion in UO_2 [30–32]. To support the development of accident tolerant fuel performance codes, for which limited experimental data exist, the same mix of atomic scale simulation techniques can be applied to predict defect diffusion in U_3Si_2. Andersson et al. have already used DFT to derive parameters for U and Si defect stability and D_1 diffusion in U_3Si_2 [33]. By studying D_1, they generated all the defect energy data necessary to parameterize the cluster dynamics framework of Matthews et al. [28, 29] for the study of D_2 diffusion in U_3Si_2.

In this work, cluster dynamics simulations for U_3Si_2 have been developed to predict point defect concentrations and diffusivities for in-reactor conditions. MD simulations, employing the Beeler U-Si potential [34], have been used to simulate athermal contributions to self-diffusion through ballistic cascades in the bulk lattice, as well as the diffusivity of U and Si at grain boundaries. These atomic-scale diffusivity data have then been combined to develop a lower length scale (LLS) informed model for Nabarro-Herring, Coble, and climb creep of U_3Si_2. The model was validated against available literature experimental data and has been implemented in the BISON fuel performance code to demonstrate its application for U_3Si_2 fuel using simple power profiles for steady-state and loss of coolant accident (LOCA) conditions.

2. Method

2.1. Cluster dynamics simulations

Single-point cluster dynamics simulations were carried out using the Centipede code developed by Matthews et al. [28, 29]. The framework has been applied to the simulation of defect concentrations and diffusivities contributing to self-diffusion [28] and Xe diffusion [29] in UO_2 under irradiation, capturing the D_1-D_2 transition for self- and Xe diffusion. A detailed description of the framework can be found elsewhere [28, 29], however a brief description of the method and its application to U_3Si_2 will be given here.

The concentrations of defects in the system are calculated by solving a set of ordinary differential equations (ODEs) that capture a number of phenomena including: production of Frenkel pairs through irradiation, mutual recombination of Frenkel pairs, interaction with sinks, and clustering of point defects. For a given defect concentration, x_d, the ODE can be expressed as:

$$\frac{dx_d}{dt} = \dot{\beta}_d + \sum \dot{R}_d(x_p, x_r, D_p, D_r, T, G) \tag{1}$$

where $\dot{\beta}_d$ describes the source rate of defects through irradiation. $\dot{R}_d$ is the rate of a reaction that acts upon defect d, and is summed across all possible reactions involving that defect. A given reaction rate depends on the concentrations of the reactants (x_r) and the products (x_p), their respective diffusivities (D_r and D_p), the temperature (T), and the free energy of the system (G). The Centipede code finds the steady-state solution to this coupled set of ODEs, such that $\frac{dx_d}{dt} \leq \mathcal{R}$ for all defects, where $\mathcal{R}$ is a convergence criterion. An individual reaction, $\dot{R}_d$, can be expressed as:

$$\dot{R}_d = \begin{cases} \frac{k_i^2}{\Omega} D x_A x_B \left[1 - exp\left(\frac{f}{k_B T}\right)\right], & \text{if } f < 0, \\ \frac{k_i^2}{\Omega} D x_Y x_Z \left[exp\left(\frac{f}{k_B T}\right) - 1\right], & \text{otherwise} \end{cases} \tag{2}$$

where Ω is the atomic volume, k_i is a reaction rate constant that depends on the distance over which two defects are assumed to interact, $D = D_A + D_B$ is the sum of the diffusivities of the reactants (labeled A and B), x_A and x_B are the concentrations of the reactants and x_Y and x_Z are the concentrations of the products (labeled Y and Z). If $f < 0$ the net rate is for the reaction to go forwards and otherwise it goes backwards. The driving force is given by the change in the free energy of the system due to the reaction:

$$f = \sum_{p \epsilon P} \frac{\partial G}{\partial x_p} - \sum_{r \epsilon R} \frac{\partial G}{\partial x_r} \tag{3}$$

where P and R are the set of products, p, and reactants, r, respectively. G is the total free energy of the system, such that the partial derivatives in Eq. (3) are dictated by the free energy of formation of the reactant and products, as well as the configurational entropy associated with their concentrations. Therefore, the key parameters needed to apply the Centipede code to U_3Si_2 are the defect formation energies and entropies, which define the driving force of various reactions, and the diffusivities of the defects, which, along with the driving force, determine the reaction rates.

Here, this framework has been applied to the simulation of irradiation-enhanced defect concentrations and diffusion in U_3Si_2. One of the key differences with the original application to UO_2

is that, due to the relatively low mobility of U and Si vacancies, the defect concentrations on both the U and Si sublattices must be tracked. Conversely, in the UO_2 system both interstitials and vacancies on the oxygen sublattice migrate so fast that interaction with sinks and mutual recombination maintains thermal equilibrium concentrations. Given that two sublattices are tracked, there are now three dependent variables that represent the perfect lattice sites: U_U, Si_{Si}, and V_i. Given that they are immobile, antisite defects are omitted to limit the number of solved variables and ODEs. The following reactions are solved for:

Reactions of U and Si defect with sinks

$$sink + U_i \leftrightarrow sink + V_i \tag{4}$$
$$sink + Si_i \leftrightarrow sink + V_i \tag{5}$$
$$sink + V_U \leftrightarrow sink + U_U \tag{6}$$
$$sink + V_{Si} \leftrightarrow sink + Si_{Si} \tag{7}$$

Annihilation of interstitials and vacancies

$$U_i + V_U \leftrightarrow U_U + V_i \tag{8}$$
$$Si_i + V_{Si} \leftrightarrow Si_{Si} + V_i \tag{9}$$

where standard Kröger-Vink notation has been used [35] but with charges omitted due to the system having metallic bonding. In previous work on UO_2 [27, 28], single vacancies were found to have a large migration barrier of 4.23 eV, while clustering to form divacancies could lower this to 2.39 eV. Despite this, irradiation-enhanced diffusion [28] was dominated by single U vacancies with no contribution from divacancy clusters. In U_3Si_2, single vacancies (and interstitials) already have comparatively small barriers [33] (see Table 2), making it unlikely that clustering will lower the migration barriers sufficiently to impact irradiation-enhanced diffusion. On that basis, clusters of vacancies and interstitials have been omitted from our simulations. Future studies, supplemented by the necessary DFT data, should assess this assumption. Radiation damage is accounted for by a source term for Si and U Frenkel pairs that is unchanged from those used for V_U and U_i in the application of Centipede to UO_2 [28, 29]. This assumes that defect production due to fission in UO_2 and U_3Si_2 are approximately equal. Similarly the sink terms used for V_U, U_i, V_{Si}, and Si_i are unchanged from the application to UO_2, which was based on the intra-granular bubbles that form [28, 29]. This assumes that sinks result in similar aggregate behavior in U_3Si_2 as in UO_2. Although there is a lack of data on U_3Si_2 to confirm these assumptions regarding the sink and source rates, a parametric study was carried out to test the impact of this uncertainty. It was found that there would be a negligible impact on final self-diffusion and creep models; however, it would still be of interest to more closely examine these assumptions in future work.

The tetragonal unit cell of U_3Si_2 is shown in Fig. 1. The two symmetrically unique U sites (2a and 4h) and the single Si site (4g) are shown. The two symmetrically equivalent interstitial sites that are active for defect formation and diffusion are identified with a cross. The defect stabilities and mobilities determine the behavior of the defects during the cluster dynamics simulations. The thermodynamic stability of the defects is given by the formation enthalpies and entropies taken from Andersson et al. [33], and are summarized in Table 1. The U_3Si_2 system contains two symmetrically unique uranium lattice sites. To simplify the cluster dynamics simulation, only the most stable V_U site (2a) was considered for the total V_U concentration. Previously, Andersson et al. treated the concentrations as per site values [33]. However, for the purposes of the cluster

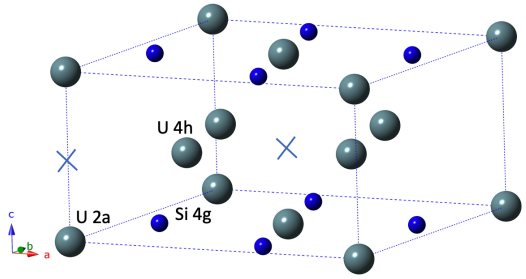

Figure 1: The tetragonal unit cell of U_3Si_2 (space group $P4/mbm$). There are two distinct U sites (2a and 4h) and a single Si site (4g). The two equivalent interstitials sites that are active in U_3Si_2 are indicated with by ×.

Table 1: Point defect formation energies and entropies, from Andersson et al. [33], used in the cluster dynamics model.

Defect	H_f (eV)	S_f (k_B)	n
U_i	0.87	-3.15	2
V_U	1.69	0.45	1
Si_i	0.55	2.19	1
V_{Si}	1.79	6.28	2

dynamics simulations it is important to account for the fact that there are not the same number of sites available to each defect in a given volume. Therefore, the concentration of the defects have been adjusted to account for the number of sites per formula unit, n. Under thermal equilibrium in the dilute limit, the defect concentration, $[x]$, of defect x is given by the Arrhenius function:

$$[x] = n \cdot \exp\left(\frac{-H_f + S_f T}{k_B T}\right) \tag{10}$$

where H_f is the enthalpy of formation, S_f is the entropy of formation, k_B is the Boltzmann constant, and T is the temperature.

In addition to the thermal stability defined by H_f, S_f, and n, the diffusivity of individual defects, D_x, must be known in order to determine the irradiation-enhanced defect concentrations. This is defined by the defect migration barrier (H_{mig}), attempt frequency (v_{mig}), number of jump directions (Z), the jump distance (α), and the dimensionality of diffusion (ξ), as such:

$$D_x = \frac{Z}{2\xi}\alpha^2 v_{mig} \exp\left(\frac{-H_{mig}}{k_B T}\right) \tag{11}$$

In U_3Si_2 there are two unique crystallographic directions for diffusion. For defining the rates within the cluster dynamics framework, the fastest of the two directions for each defect was taken from Andersson et al. [33] and the relevant parameters are summarized in Table 2.

Table 2: Parameters that describe the defect diffusivities, from Andersson et al. [33], used in the cluster dynamics model.

Defect	H_{mig} (eV)	v_{mig} (Hz)	α (Å)	ξ	Z
U_i	0.31	1.51×10^{14}	3.80	2	4
V_U	1.21	1.40×10^{13}	3.90	1	2
Si_i	1.80	1.00×10^{13}	5.18	2	4
V_{Si}	2.37	1.00×10^{13}	4.19	2	4

2.2. Molecular dynamics simulations

2.2.1. Potential model

MD simulations were carried out using the Large-scale Atomic/Molecular Massively Parallel Simulator (LAMMPS) code [36]. The description of U-Si and Si-Si interatomic forces is given by the modified embedded atom method (MEAM) potential developed by Beeler et al. [34] and was developed to be used with the U-U interactions derived by Moore et al. [37]. The MEAM potentials are splined to a Ziegler-Biersack-Littmark (ZBL) potential [38] in the standardized method implemented in LAMMPS. The potential was fitted to structural properties, phase stability, elastic constants, and defect formation energies for various uranium silicide compounds. A particular focus was given to the accurate description of the properties of U_3Si_2. Beeler et al. demonstrated the potential for 1 keV ballistic damage cascades [34].

2.2.2. Athermal diffusion

For the damage cascade simulations, a large U_3Si_2 supercell, consisting of a 30×30×50 extension of the unit cell, was used to restrict the possibility of the cascade overlapping the periodic boundaries. The system was equilibrated at 600 K for 15 ps in the NPT ensemble at zero pressure, using Nosé-Hoover barostat and thermostat relaxation times of 0.1 ps and 0.5 ps, respectively, and a 2 fs timestep. During the final 5 ps of equilibration the cell dimensions were averaged. The final equilibrated system was re-scaled and fixed to the averaged cell dimensions to mitigate volumetric fluctuations and was then used as the starting point for subsequent damage simulations.

Cascade simulations were carried out in the NVE ensemble using the supercell dimensions that were equilibriated at 600 K. The cascades were initialized by selecting a U atom at random and scaling its velocity in a random direction with a kinetic energy of 1 keV, 2 keV, or 3 keV. Given the high atomic velocities involved, control of the timestep is necessary to ensure accurate integration over the potential energy surface. Sufficient numerical accuracy has been defined so that the total energy of the system is constant between timesteps, thus, satisfying conservation of energy. To achieve this a 0.001 fs timestep was used for the first 0.5 ps, followed by 0.003 fs for 3 ps, then 0.01 fs for 10 ps, and 0.1 fs for the remaining 16.5 ps. These are notably small timesteps even for a cascade simulation and indicate a potential energy surface for U_3Si_2 with which care should be taken to ensure accurate integration. For PKA energies of 4 keV and greater, the required timestep became small enough to make the cascade simulations too computationally challenging. We have, therefore, assumed the MSD during low energy cascades can be extrapolated to high energy. The cascades were repeated 3 times for each PKA energy with a different random PKA direction taken each time. The MSD was averaged over the final 15 ps and over the 3 repetitions to determine the MSD as a function of PKA energy. Although the temperature was not sufficiently

high for intrinsic diffusion, the atomic vibrations of bulk atoms at their original sites made a non-negligible contribution to the MSD. Therefore, the MSD due to atoms moving from their initial positions but remaining in same potential well (atomic site) was calculated for the system at 600 K and subtracted from the MSD in the cascade simulations.

2.2.3. Grain boundary diffusion

MD simulations were used to study self-diffusion at grain boundaries. The objective of these simulations was to get a first estimate of the differences in diffusivities at the grain boundary, as opposed to the bulk, to ensure our final creep model accounts for a broad range of phenomena. Only a single grain boundary has been studied here and future work may consider a more comprehensive set of grain boundaries, such as those examined by Beeler et al. in their study of grain boundary and surface energies [39]. A Σ-530 tilt grain boundary structure was used with a grain size of 83.6 nm. To ensure sufficient statistics, a supercell consisting of 480,000 atoms was created by extension in the directions parallel to the grain boundary. The system was equilibrated at the temperature of interest (1200 K to 1600 K at 100 k intervals) for 15 ps in the NPT ensemble at zero pressure, using barostat and thermostat relaxation times of 0.1 ps and 0.5 ps, respectively, and a 1 fs timestep. The supercell dimensions were averaged over the final 5 ps. By fixing the supercell at the averaged dimensions, the system was allowed to continue evolving in an NVT ensemble at the temperature of interest for 3 ns, during which the MSD of U and Si atoms was computed. As discussed in greater detail in Section 3.2, the slope of the MSD as a function of time for the final 1 ns was used to calculate the diffusivities of U and Si at the grain boundary. The simulation time was determined by assessing the MSD vs time to ensure a linear relationship when fitting the diffusion coefficient. Figure 2 shows the MSD vs time for the supercell containing two grain boundaries at the two lowest temperatures studied: 1200 K and 1300 K. It can be seen that it was necessary to run the simulations for 3 ns to achieve a significant period of time (1 ns) where a linear relationship was obtained. At shorter timescales the MSD was overly-heavily influenced by fast short-range pathways that do not contribute to diffusion over long timescales. The linear relationship between 2 ns and 3 ns indicates the true diffusion coefficient was achieved. Two defective grain boundary supercells, where 0.34% of the Si or U atoms were deleted at random, were also examined, however, only a negligible effect on the diffusivity was noticed. This indicates that the grain boundary diffusivity was not sensitive to vacancies and that bulk vacancy diffusion was far less significant than the contribution from U and Si atoms in the grain boundary itself.

2.3. BISON simulations

To examine the extent of U_3Si_2 creep for in-reactor conditions, a small 10-pellet fuel rodlet was analyzed using the BISON fuel performance code. The cladding is taken as Zircaloy-4. The rodlet was modeled using a 2D-RZ axisymmetric representation of the fuel and cladding. Tabel 3 lists the geometry of the rodlet, initial conditions of the fill gas, and the operational conditions of the coolant (representative of a PWR). The LLS-informed creep model developed in Section 3.3 was used. The power supplied to the fuel was linearly increased from zero to its maximum value over 10,000 seconds for the fresh fuel cases. It was then held at the maximum values for 3.2 years. Initially, a maximum power rating of 20 kW/m, which is typical of a LWR, was used; however, negligible creep was predicted, due to the high thermal conductivity of U_3Si_2 resulting in low temperatures. In this work, we use a maximum power rating of 35 kW/m at steady state conditions to examine if significant creep occurs at higher temperatures (see Section 3.4).

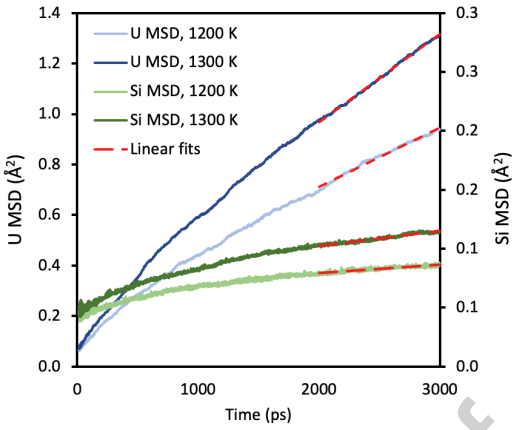

Figure 2: The MSD of U (left axis) and Si (right axis) for the supercell containing two Σ530 grain boundaries. The fits over the final 1 ns that were used to calculate the diffusion coefficients are shown using red dashed lines.

In addition to the baseline cases using constant power, the behavior during a LOCA was also tested. To simulate a LOCA following the initial base irradiation, the fuel was subjected to a temperature transient applied to the outer cladding surface that was consistent with furnace tests completed at Studsvik [40, 41]. An axial temperature profile of $20\sin(x\pi/L) + T_{in}$ was applied, whereby x is the axial position, L is the rod length, and T_{in} is the inlet temperature, such that the peak temperature is 20 K higher than at the ends of the rod. This profile provides the driving force for ballooning of the cladding.

Table 3: Rodlet specifications for normal operation simulation

	Value	Units
Number of pellets	10	-
Fuel enrichment	5	%
Pellet length	9.83	mm
Pellet outer diameter	8.19	mm
Radial gap width	82.55	μm
Clad thickness	0.572	mm
Rodlet diameter	9.5	mm
Initial fill pressure	2	MPa
Initial fill gas	Helium	-
Plenum height	26	mm
Initial fuel grain size	20	μm
Coolant inlet mass flux	3800	kg/m^2-s
Coolant inlet temperature	580	K
Coolant pressure	15.5	MPa

3. Results and Discussion

3.1. Bulk self-diffusion

There are three possible contributions to the diffusion of point defects in bulk U_3Si_2: i) thermal equilibrium diffusion (D_1), ii) irradiation-enhanced diffusion (D_2), and iii) athermal atomic mixing during cascades (D_3). The diffusion of point defects under thermal equilibrium conditions (D_1) has been studied by Andersson et al. [33]. In Section 3.1.1, we show the results of implementing the point defect stabilities and diffusivities from Andersson et al. [33] in cluster dynamics simulations to predict irradiation-enhanced diffusion (D_2). In Section 3.1.2, results are shown from MD simulations of ballistic cascades to examine the athermal contribution of atomic mixing to diffusion (D_3).

3.1.1. Thermal equilirbium D_1 and irradiation-enhanced D_2 diffusion

In this section the Centipede cluster dynamics code of Matthews et al. [28, 29] has been applied to investigate the D_2 regime in U_3Si_2, where thermally activated diffusion is mediated by irradiation-enhanced defect concentrations. The defect free energies are defined by the DFT data calculated by Andersson et al. [33], which includes the energies of all reactions involved in the cluster dyanamics model (as shown in Eqs. (4) to (9)).

The concentrations of V_U, U_i, V_{Si}, and Si_i under irradiation conditions, assessed using cluster dynamics, are shown in Fig. 3a. At high temperatures, all defects are at their thermal equilibrium concentrations and Si_i are highest in concentration followed by V_{Si}, then U_i, then V_U. As the temperature decreases, irradiation-enhancement of first V_{Si} (<870 K), then V_U (<700 K), and then Si_i (<650 K), occurs. These enhanced concentrations will influence the low temperature creep rate, as studied in Section 3.3. The concentration of U_i does not undergo irradiation-enhancement. This is due to its very low migration barrier of 0.31 eV, which ensures it has a sufficiently high mobility to annihilate with V_U and sinks even at the lowest temperature studied here.

By converting the defect concentrations shown in Fig. 3a to per U atom and per Si atom quantitites and then multiplying by the diffusivities of the defects in the fastest crystallographic direction (given by Eq. (11) and the parameters in Table 2), the contributions from different point defects to U and Si self-diffusivity have been determined, as shown in Fig. 3b. As expected from previous work [33], it can be seen that the self-diffusivity due to interstitials is much greater than that due to vacancies. Additionally, the irradiation-enhanced regime for vacancies is broadly athermal, except for the lowest temperature studied (600 K). Fig. 3b also shows a proportional relationship between the fission rate density and the irradiation-enhanced regime. Correlations based on the data given in Fig. 3b for the contribution of each defect to U and Si self-diffusion are as follows:

$$D_{V_U}^{self} = 1.113\times10^{-6}\cdot\exp\left(\frac{-2.900\text{ eV}}{k_BT}\right) + 1.770\times10^{-46}\dot{F} \quad \text{m}^2\text{s}^{-1} \tag{12}$$

$$D_{U_i}^{self} = 1.869\times10^{-6}\cdot\exp\left(\frac{-1.180\text{ eV}}{k_BT}\right) \quad \text{m}^2\text{s}^{-1} \tag{13}$$

$$D_{V_{Si}}^{self} = 9.371\times10^{-4}\cdot\exp\left(\frac{-4.160\text{ eV}}{k_BT}\right) + 1.971\times10^{-47}\dot{F} \quad \text{m}^2\text{s}^{-1} \tag{14}$$

$$D_{Si_i}^{self} = 2.397\times10^{-5}\cdot\exp\left(\frac{-2.350\text{ eV}}{k_BT}\right) \quad \text{m}^2\text{s}^{-1} \tag{15}$$

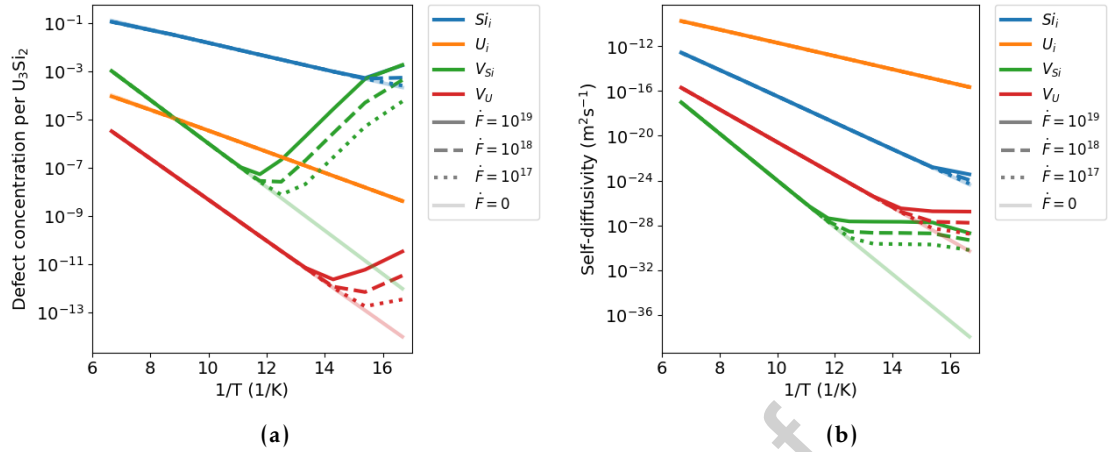

Figure 3: a) The irradiation-enhanced point defect concentrations per U_3Si_2 formula unit from cluster dynamics simulations. b) The contributions of various point defects to irradiation-enhanced self-diffusivity in U_3Si_2 from cluster dynamics simulations. The results include contributions from D_1 and D_2 type diffusion for $\dot{F}$ of 10^{19} $m^{-3}s^{-1}$, 10^{18} $m^{-3}s^{-1}$, 10^{17} $m^{-3}s^{-1}$, and 0 $m^{-3}s^{-1}$.

where the first terms in Eqs. (12) to (15) represent thermal equilibrium D_1 diffusion, while the second terms, if present, represent irradiation-enhanced D_2 diffusion. These results are the contributions of the defects to self-diffusion and, as discussed later, this is different from the diffusivities used for Nabarro-Herring creep (where the rate limiting crystallographic direction is dominant).

As discussed previously, the sink and source terms were carried over from UO_2. This assumption was a practical consideration due to the lack of U_3Si_2 data for the production of Frenkel pairs and sink evolution under irradiation. In order to address the impact of these assumptions for studying irradiation-enhanced self-diffusion and creep in U_3Si_2, a parametric study has been performed by varying the sink and source terms by an order of magnitude in each direction with respect to the baseline case studied so far. Figure 4a shows that varying the sink rate has a negligible impact on the defect concentrations above 700 K. There is a small change in the defect concentrations below 700 K. Figure 4b shows the impact of varying the source term by several orders of magnitude. Similar to the fission rate dependence, the defect concentrations in the irradiation-enhanced regime (D_2) scale linearly with the source term. It will be shown in Section 3.1.2 that the athermal D_3 contribution for self-diffusivity is 4, or more, orders of magnitude greater than the D_2 terms. Additionally, in Section 3.3, the creep rates that result from D_2 irradiation-enhanced diffusion were found to be negligible and did not make a significant contribution to pellet creep for in-reactor conditions (see Section 3.4). Therefore, the uncertainties associated with the sink and source terms are not expected to impact our results for the development of self-diffusion and creep models for U_3Si_2 nuclear fuel. For similar reasons, we do not expect the assumption that clustering does not occur in U_3Si_2 to have an impact on our final results. Although, this would be an interesting topic for future studies.

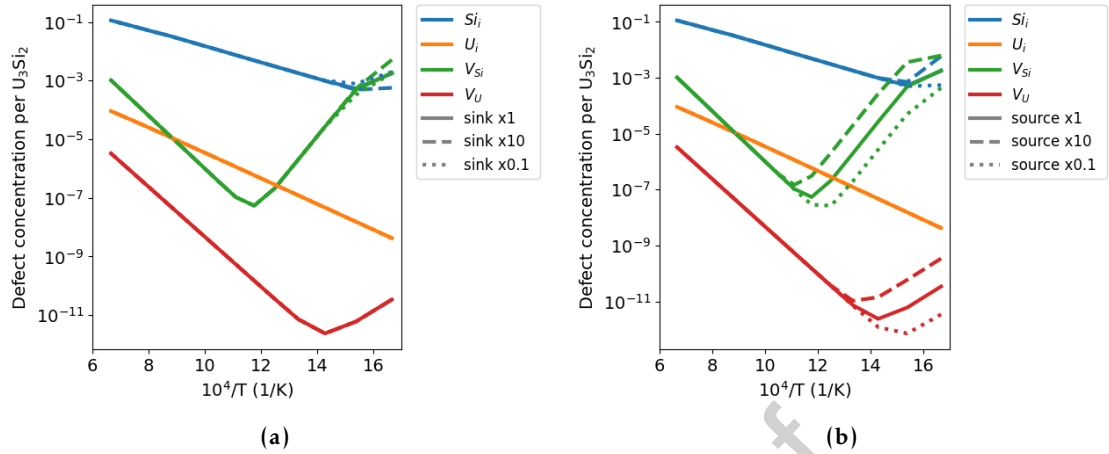

Figure 4: A parametric study of the impact of the a) sink and b) source strengths on the irradiation-enhanced point defect concentrations per U_3Si_2 formula unit from cluster dynamics simulations.

3.1.2. Athermal D_3 diffusion

To simulate atomic mixing during the ballistic stopping of high energy fission fragments (responsible for athermal diffusion), damage cascade simulations were carried out. It was found that damage cascade simulations on this system required significantly smaller timesteps than usual. As such, PKA energies of 4 keV and above were not practical. PKA energies of 1 keV, 2 keV, and 3 keV were simulated, enabling the trend as a function of PKA energy to be identified. Figure 5a shows the MSD of Si and U in U_3Si_2 as a function of time during a 3 keV ballistic cascade at 600 K. There was an initial rapid increase in atomic displacement that is maintained as atoms come to a rest some distance away from their initial positions.

Figure 5b shows the MSD of U and Si in U_3Si_2 averaged over the final 15 ps of the simulation as a function of the PKA energy deposited per unit volume at 600 K. The data in Figure 5b has been averaged over 3 randomly orientated ballistic cascades for each PKA energy. The PKA energy deposited per unit volume is analogous to the heating density due to fission and will be used later to determine the athermal diffusion coefficient. It can be seen from Fig. 5b that greater displacement is predicted for U than Si. In previous work on UO_2 [32], O displacement greatly exceeded that of U. It was speculated that the difference between U and O could be attributed either to the higher migration barriers and formation energies for U defects or to the much greater mass of U corresponding to lower velocities during mixing. However, in U_3Si_2 displacement by ballistic cascades follows the same ordering as for the intrinsic diffusivities predicted by DFT (U>Si) [33] and bears no correlation to the inverse of the atomic mass of the species (Si>U). This supports the conclusion that in both systems the formation and mobility of the defects is more indicative of the extent of atomic mixing than is the mass of the species. However, it should be noted that for U_3Si_2 the differences in the MSD of U and Si are small enough that it could be down to statistical variation or approximations inherent to the use of an empirical potential. Similar predictions were made by Beeler et al. [43] for athermal diffusion in UMo alloy, in that U and Mo have similar diffusivities.

The derivation of diffusivity from cascade simulations used here is analogous to that discussed

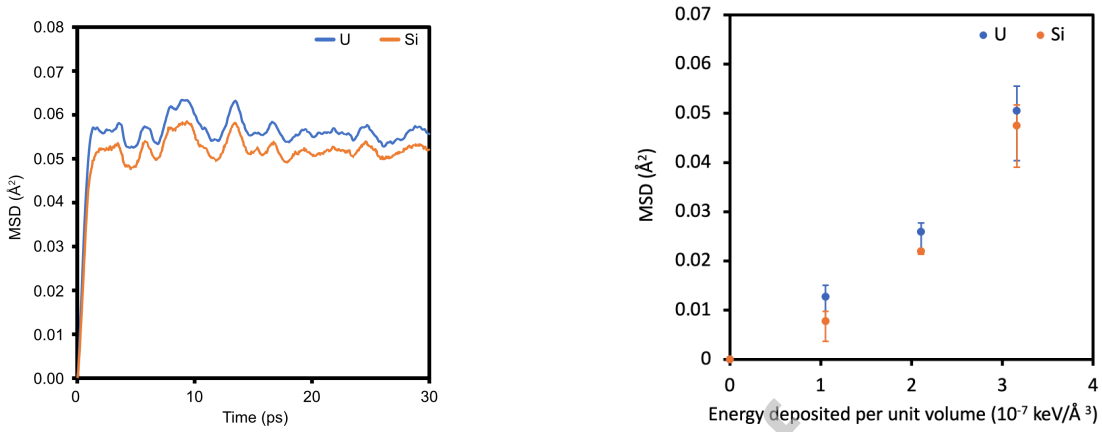

Figure 5: a) The MSD of U (blue) and Si (orange) as a function of time during a 3 keV damage cascade in U_3Si_2 at 600 K. b) The MSD of U (blue), and Si (orange) averaged over the final 15 ps of cascade simulations at 600 K as a function of the PKA energy deposited per unit volume. Each point is the average of 3 such cascade simulations. The range of MSD values obtained for the three repetition at each PKA energy are represented by the errors bars.

previously [32, 43]. During fission a U atom splits into two high energy fission fragments characterized by a bi-modal distribution of the fission yield as a function of the fission fragment mass. On average the heavy fission fragment has 70 MeV of kinetic energy and the light fission fragment has 100 MeV. As the fission fragments travels through the lattice they experience drag (stopping) through interaction with the surrounding lattice. Initially traveling at high velocity, they interact most strongly with the electrons depositing 90% of their initial energy electronically (based on the value for UC being representative of U_3Si_2, using the same assumption as in Ref. [44]). Due to the high thermal conductivity of U_3Si_2 [3], it is assumed all energy that has been deposited electronically dissipates before atomic mixing can occur through a thermal spike. Having slowed sufficiently, fission fragments deposit the remaining 10% of their initial energy by interaction directly with the lattice through the creation of PKAs (as simulated here).

Typically diffusion occurs through thermal random walk, however, an equivalent diffusion coefficient, D_3, based on atomic mixing during irradiation can be determined:

$$D_3 = D_B + D_E \tag{16}$$

where D_B and D_E are the athermal diffusivity contributions from ballistic and electronic stopping, respectively. As discussed previously, electronic stopping is omitted ($D_E = 0$) due to the high thermal conductivity exhibited by the metallically-bonded U_3Si_2. Therefore,

$$D_3 = A\dot{F} \tag{17}$$

$$A = \frac{0.1}{6}\epsilon_B E_F \tag{18}$$

Table 4: The ϵ_B, A_B, and D_3 parameters for U_3Si_2 from Eqs. (16) to (18). E_F is taken to be 170 MeV and it is assumed 10% of this energy is deposited through ballistic stopping. D_3 values assume a fission rate density of 10^{19} $m^{-3}s^{-1}$. These assumptions can be modified depending on reactor design or local irradiation conditions.

Species	ϵ_B (m^5MeV^{-1})	A_B (m^5)	D_3 (m^2s^{-1})
U	1.46×10^{-42}	4.15×10^{-42}	4.15×10^{-23}
Si	1.32×10^{-42}	3.73×10^{-42}	3.73×10^{-23}

where $\dot{F}$ is the fission rate per unit volume, and A is the constant of proportionality between D and $\dot{F}$. The MSD per unit energy deposited in a unit volume of lattice during ballistic stopping is given by ϵ_B, and is taken as the slope of a linear fit to the data in Fig. 5b. A linear relationship was selected due to the narrow range of PKA energies examined and the possibility of unphysical extrapolation of a non-linear function, particularly if there is noise in our data (as captured by the error bars in Fig. 5b). Future work could examine, in more detail, the relationship shown in Fig. 5b to higher PKA energies. The weighting factor of 0.1 is based on the proportion of fission energy, E_F, deposited ballistically rather than electronically, taken from Ref. [44].

Table 4 shows the values of ϵ_B calculated at 600 K for U and Si. Note that we treat these values of ϵ_B as valid for all temperatures, given that this mechanism was shown to be broadly athermal in UO_2 and UMo [32, 43]. The parameter ϵ_B can be considered as the efficiency of the mechanism in converting energy into atomic displacement. There is only marginal variation in ϵ_B between U and Si. Table 4 shows ϵ_B, A, and D for U and Si. Our calculations of A and D are based on assumptions about the irradiation environment and radiation-material interactions. If one wishes to do so, different assumptions based on alternative irradiation environments (e.g. spent nuclear fuel storage conditions) can be used in conjunction with ϵ_B. Alternatively, these parameters could be coupled with fuel performance simulations to give the local diffusivity based on the fission rate density in a specific part of the reactor or radial position in the pellet.

The contribution to self-diffusion from D_3 is several orders of magnitude larger than the D_2 diffusion terms calculated for V_{Si} and V_U in Eqs. (12) and (14). As such, in contrast to the behavior observed for UO_2 [45], self-diffusion is dominated by D_1 and D_3 contributions only.

3.2. Diffusivity at the grain boundary

Self-diffusivity at grain boundaries is an important parameter that contributes to several phenomena that impact fuel performance, such as inter-granular bubble swelling. It is also the key parameter that governs the kinetics of Coble creep (as will be examined in more detail in Section 3.3.2). Following the procedure outlined in Section 2.2.3, a system containing two Σ-530 grain boundaries (in the x-z plane) was equilibrated at various temperatures for 100 ps. Subsequently, the MSD in each direction orthogonal to the simulation cell was calculated for another 3 ns. In this section, we are interested in determining diffusivity specifically at the grain boundary itself. Therefore, we calculated the MSD for the perfect lattice at temperatures ranging from 1200 K to 1600 K, finding that no diffusion occurred on these timescales. As such, it can be assumed that all of the displacement that occurs in the grain boundary simulations is due only to displacement of atoms within the grain boundary. To convert the MSD for the entire supercell, $< r^2 >_{supercell}$, into a grain boundary specific MSD, $< r^2 >_{GB}$, a scaling factor based on the thickness of the grain boundary compared to the supercell length perpendicular to the grain boundary, L_Y,

has been applied, as follows:

$$< r^2 >_{GB} = \frac{L_Y}{4\delta} < r^2 >_{supercell} \tag{19}$$

where δ is the distance from the center of the grain boundary to the point where the lattice has bulk characteristics. The factor of 4 takes into account that this thickness applies to either side of the center of the grain boundary and that there are two grain boundaries in the supercell. δ is taken to be 1 nm, however, as will be shown later, when calculating the Coble creep rate δ is canceled out.

The derivative of $< r^2 >_{GB}$ with respect to time, t, was calculated by a linear fit to the MSD data from 2 ns to 3 ns. The diffusivity is given by:

$$D_{GB} = \frac{1}{2\xi} \frac{d < r^2 >_{GB}}{dt} \tag{20}$$

where ξ is the dimensionality being considered when calculating D, such that $\xi = 1$ for diffusivity in 1D (i.e. D_x, D_y, and D_z). Therefore, the diffusivity in the x-z plane of the grain boundary, $D_{GB_\parallel}$, is given by applying Eq. (20) to the 2D case, where $< r^2 >_{GB} = < x^2 >_{GB} + < z^2 >_{GB}$ and $\xi = 2$.

Figure 6 shows $D_{GB_\parallel}$ for U and Si in U_3Si_2 as function of temperature. It can be seen that the grain boundary diffusivity of U is greater than that of Si. It is also noted that when the system was seeded with Si and U vacancies no change in grain boundary diffusivity was seen beyond what is typical of statistical variation between two simulations; consequently, the impact of point defect concentration on grain boundary self-diffusion has been omitted from further analysis. For the purposes of developing a grain boundary (Coble) creep model for U_3Si_2 fits to the data shown in Fig. 6 will be used. Arrhenius functions for U and Si grain boundary diffusion are, thus, given by:

$$U: \quad D_{GB_\parallel} = 1.562 \times 10^{-6} \exp\left(\frac{-1.404 \text{ eV}}{k_B T}\right) \quad \text{m}^2\text{s}^{-1} \tag{21}$$

$$Si: \quad D_{GB_\parallel} = 6.411 \times 10^{-7} \exp\left(\frac{-1.619 \text{ eV}}{k_B T}\right) \quad \text{m}^2\text{s}^{-1} \tag{22}$$

where these functions are also shown in Fig. 6 alongside the MD data. It is noted that there is some deviation from linearity in Fig. 6, which we attribute to the complex structure of the grain boundary. This results in many different migration pathways that, due to a range of activation energies, contribute to diffusion to a greater or less extent for different temperatures. In order to study this more carefully, MD simulations to lower temperatures would be necessary. However, insufficient displacement occurred below 1200 K on the ns-timescales used in this study.

3.3. Creep model

In this section, we use the atomistic data for thermal equilibrium and irradiation-enhanced bulk diffusion, and grain boundary diffusion to derive correlations for creep mechanisms that are governed by point defect kinetics, namely: i) Nabarro-Herring creep, ii) Coble creep, and iii) dislocation climb.

3.3.1. Nabarro-Herring creep

The defect concentrations calculated from the cluster dynamics simulations can be analyzed to understand thermal and irradiation-enhanced contributions to bulk diffusional creep (Nabarro-Herring creep). Nabarro-Herring creep is due to the diffusion of point defects under an elastic

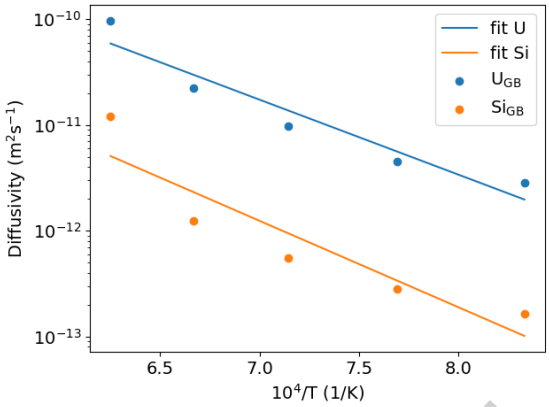

Figure 6: The diffusivity of U (U_{GB}) and Si (Si_{GB}) at a Σ-530 tilt grain boundary, $D_{GB_\parallel}$, predicted using MD simulations. The fits to the MD data given by Eqs. (21) and (22).

strain. The direction of the diffusion of a point defect is determined by the sign of the defect volume (change in lattice volume upon formation of the defect). Defects that contract (expand) the lattice are more favorably in regions of compressive (tensile) strain. Given that in U_3Si_2 vacancies (interstitials) contract (expand) the lattice, the flow of mass is from the compressive to the tensile region of a grain (the defect volumes from Ref. [33] used here are summarized in Table 5). Therefore, bulk diffusion under a stress gradient enables plastic deformation (creep) that acts to relieve an applied stress.

The equivalent Nabarro-Herring creep rate, $\dot{\epsilon}_{NH,\,x}$, due to a given defect, x, is expressed as [46, 47]:

$$\dot{\epsilon}_{NH,\,x} = \frac{42|\Omega_x|D_x[x]}{k_B T d^2}\sigma_v \tag{23}$$

where σ_v is the Von-Mises stress, and d is the grain size. $[x]$ and Ω_x are the defect concentration (calculated in Section 3.1.1) and volume, respectively. D_x is the diffusivity of the defect. Due to the anisotropic nature of the U_3Si_2 system, D_x must be selected carefully. Although more generally the defects will diffuse according to the specific tensile and compressive fields within the medium, for simplicity we have assumed that for Nabarro-Herring creep, diffusion of point defects must occur from one side of the grain to a perpendicular (not opposite) side. This requires the defect to traverse both the aa and cc crystallographic directions. Diffusion in a single direction would not result in creep. Therefore, the direction of slowest mobility will be rate-limiting. As such, the defect diffusivities used for creep are different to those used to assess the defect concentrations during cluster dynamics simulations, and are given in Table 5.

Whereas Nabarro and Herring considered the current due to a single vacancy species, here we must also consider the role of interstitials, due to their low formation energy and high mobility. Furthermore, both U and Si defects must be included and care is taken to ensure only stoichiometric redistribution of material can occur. Separate contributions from different defects to Nabarro-Herring creep were assessed using Eq. (23) with the defect concentrations from Sec-

Table 5: Parameters describing defect diffusivities, from Andersson et al. [33], used in the Nabarro-Herring creep model. Migration barriers, H_{mig}, attempt frequencies, v_{mig}, dimensionality, ξ, jump distance, α, number of jump sites, Z, and the defect volumes, Ω_x, are reported.

Defect	H_{mig} (eV)	v_{mig} (Hz)	α (Å)	ξ	Z	Ω_x (Å^3)
U_i	2.56	1.00×10^{14}	3.90	1	2	0.07
V_U	1.71	8.18×10^{12}	5.18	2	4	-4.17
Si_i	2.91	1.00×10^{13}	3.90	1	8	4.09
V_{Si}	2.44	1.00×10^{13}	4.19	1	2	-7.81

tion 3.1.1, resulting in the following expressions:

$$\dot{\epsilon}_{NH,\,V_U} = \frac{\sigma_v}{d^2T}\cdot\left[1.457\times10^{-11}\cdot\exp\left(\frac{-3.400\text{ eV}}{k_BT}\right)+5.081\times10^{-51}\dot{F}\cdot\exp\left(\frac{-0.540\text{ eV}}{k_BT}\right)\right] \tag{24}$$

$$\dot{\epsilon}_{NH,\,U_i} = \frac{\sigma_v}{d^2T}\cdot 5.912\times10^{-14}\cdot\exp\left(\frac{-3.390\text{ eV}}{k_BT}\right) \tag{25}$$

$$\dot{\epsilon}_{NH,\,V_{Si}} = \frac{\sigma_v}{d^2T}\cdot\left[1.919\times10^{-8}\cdot\exp\left(\frac{-4.230\text{ eV}}{k_BT}\right)+5.958\times10^{-51}\dot{F}\cdot\exp\left(\frac{-0.090\text{ eV}}{k_BT}\right)\right] \tag{26}$$

$$\dot{\epsilon}_{NH,\,Si_i} = \frac{\sigma_v}{d^2T}\cdot 2.161\times10^{-10}\cdot\exp\left(\frac{-3.420\text{ eV}}{k_BT}\right) \tag{27}$$

where σ_v is the Von-Mises stress in Pa, T is the temperature in K, d is the grain size in m, $\dot{F}$ is the fission rate density in $\text{m}^{-3}\text{s}^{-1}$, and the strain rate, $\dot{\epsilon}$, is given in s^{-1}.

Figure 7 shows the Nabarro-Herring creep rate due to various defects assuming $\dot{F} = 10^{19}\ \text{m}^{-3}\text{s}^{-1}$ and σ = 50 MPa. Given that the crystallographic direction with lower diffusivity is used for Nabarro-Herring creep, the interstitial contributions are greatly lowered with respect to that of the vacancies (as compared to their relative self-diffusivities, Fig. 3b, which used the highest diffusivity direction). Note that only vacancy contributions have an irradiation-enhanced contribution, in line with the concentrations shown in Fig. 3a. For both Si and U, the dominant mechanism at low temperatures is irradiation-enhanced vacancies. However, the irradiation-enhanced contribution is so low that it will result in negligible creep. At high temperatures, U vacancies and Si interstitials dominate.

The potential Nabarro-Herring creep rate for a given species is determined by the sum of the interstitial and vacancy contributions. However, for stoichiometric redistribution of material both U and Si must diffuse. Therefore, the rate limiting factor for all temperatures studied is U creep and the U_3Si_2 Nabarro-Herring creep rate in U_3Si_2 is given by:

$$\dot{\epsilon}_{NH} = \dot{\epsilon}_{NH,\,V_U} + \dot{\epsilon}_{NH,\,U_i} \approx \dot{\epsilon}_{NH,\,V_U} \tag{28}$$

3.3.2. Coble creep

The other contribution to diffusional creep is due to grain boundary diffusion (Coble creep). In Section 3.2, MD simulations were carried out to predict the grain boundary diffusivity of U and

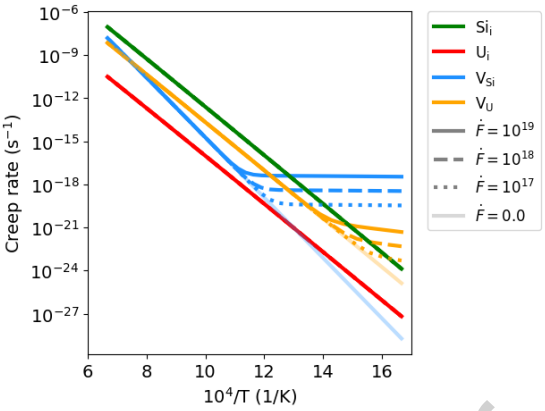

Figure 7: The Nabarro-Herring creep rate due to various point defects in U_3Si_2 as described by Equations (24) to (27) with $\sigma = 100$ MPa. Three fission rates are shown, whereby $\dot{F} = 10^{19}$, 10^{18}, and 10^{17} m^{-3}s^{-1}.

Si. The contribution to Coble creep for a given defect, x, is then given by [23]:

$$\dot{\epsilon}_{Coble,\,x} = \frac{42|\Omega_x| D_{GB} \pi \delta}{k_B T d^3} \sigma_v \tag{29}$$

where $D_{GB_\parallel}$ is given by Eqs. (21) and (22), δ is the grain boundary thickness (assumed to 1 nm). Other parameters have the same definition as in Eq. (23). The resulting Coble creep rates for each defect are as follows:

$$\dot{\epsilon}_{Coble,\,V_U} = \frac{\sigma_v}{d^3 T} \cdot 6.228 \times 10^{-20} \cdot \exp\left(\frac{-1.404\ \text{eV}}{k_B T}\right) \tag{30}$$

$$\dot{\epsilon}_{Coble,\,U_i} = \frac{\sigma_v}{d^3 T} \cdot 1.046 \times 10^{-21} \cdot \exp\left(\frac{-1.404\ \text{eV}}{k_B T}\right) \tag{31}$$

$$\dot{\epsilon}_{Coble,\,V_{Si}} = \frac{\sigma_v}{d^3 T} \cdot 4.787 \times 10^{-20} \cdot \exp\left(\frac{-1.619\ \text{eV}}{k_B T}\right) \tag{32}$$

$$\dot{\epsilon}_{Coble,\,Si_i} = \frac{\sigma_v}{d^3 T} \cdot 2.507 \times 10^{-20} \cdot \exp\left(\frac{-1.619\ \text{eV}}{k_B T}\right) \tag{33}$$

where the strain rate is given in s^{-1}.

Figure 8 shows the Coble creep rate for each defect as described by Eqs. (30) to (33). As before, the potential creep rate for a given species is determined by the sum of the vacancy and interstitial contributions. Unlike Nabarro-Herring creep, coble creep is rate limited by silicon defects due to their lower grain boundary diffusivity. Therefore, the U_3Si_2 Coble creep rate is given by as such:

$$\dot{\epsilon}_{Coble} = \dot{\epsilon}_{Coble,\,V_{Si}} + \dot{\epsilon}_{Coble,\,Si_i} \tag{34}$$

3.3.3. *Dislocation climb*

The arrival of vacancies at dislocations controls the rate at which they are able to climb over obstacles, freeing them and enabling them to glide. Therefore, the creep rate due to dislocation

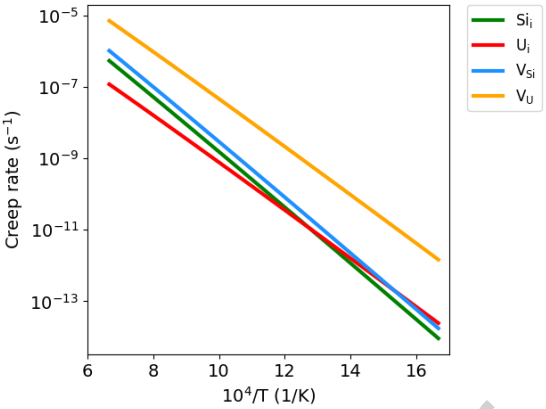

Figure 8: The Coble creep rate due to various point defects in U_3Si_2 as described by Eqs. (30) to (33) with $\sigma = 100$ MPa.

climb can be written in terms of the vacancy diffusivity, D_v, as follows [48]:

$$\dot{\epsilon}_{Climb} = A_1 \frac{D_v[x]\mu b}{k_B T}\left(\frac{\sigma_v}{\mu}\right)^3 \tag{35}$$

where μ is the shear modulus (taken as 50 GPa from Ref. [49]), b is the burgers vector (estimated here as the average lattice parameter of U_3Si_2, 5.6 Å), and A_1 is a dimensionless constant of proportionality of the order of unity (taken in this work to be exactly 1). Equation (35) represents the simplest form of the climb equation and it is not uncommon that in practice the exponent for stress will exceed 3. Due to limited data available to validate our U_3Si_2 models we have selected to leave the power law exponent as 3. Future work should revisit this as more data becomes available and the underlying models become more sophisticated. The ability of a vacancy to activate the climb mechanism is independent of the crystallographic direction it arrives along, therefore D_v is based on the higher mobility lattice direction (as described by the parameters in Table 2). As for Nabarro-Herring creep the defect concentrations, $[x]$, are taken from the cluster dynamics simulations and, therefore, account for irradiation effects. The slowest of V_{Si} or V_U was taken to be the rate limiting defect. The correlation for the creep rate due to dislocation climb is, thus, given by:

$$\dot{\epsilon}_{Climb} = \frac{\sigma^3}{T}\cdot\left(1.512\times10^{-11}\cdot\exp\left(\frac{-4.160\text{ eV}}{k_B T}\right) + 4.696\times10^{-55}\dot{F}\cdot\exp\left(\frac{0.020\text{ eV}}{k_B T}\right)\right) \tag{36}$$

where the strain rate has units of s^{-1}.

3.3.4. Validation of creep model

To test the accuracy of our model, validation has been carried out against literature compression creep tests [49]. Figure 9 shows an Ashby plot where the color indicates the relative contribution of Nabarro-Herring (red), Coble (green), and climb (blue) creep at a given stress and temperature. As expected, Coble creep dominates at low temperatures and low stresses, while dislocation

Table 6: Comparison of the model against creep tests on U_3Si_2 [49]. Experimental temperatures (T), stresses (σ), and strain rates ($\dot{\epsilon}_{Expt.}$) are provided in Ref. [49]. The strain rates from our model ($\dot{\epsilon}_{Model}$) are also reported for the same conditions.

Creep test	σ (MPa)	T (K)	$\dot{\epsilon}_{Expt.}$ (s^{-1})	$\dot{\epsilon}_{Model}$ (s^{-1})
1	44.10	1218.37	8.7327×10^{-8}	5.3136×10^{-8}
2	71.77	1205.18	1.1134×10^{-7}	8.3291×10^{-8}
4	77.68	1122.24	1.9769×10^{-8}	2.5066×10^{-8}
5	57.69	1210.10	5.2848×10^{-8}	6.6500×10^{-8}
6	46.81	1173.58	1.9071×10^{-8}	3.0276×10^{-8}
7	45.65	1223.59	4.6836×10^{-8}	5.9858×10^{-8}
9	49.43	1223.56	2.8543×10^{-8}	6.6393×10^{-8}
11	27.36	1223.70	1.1998×10^{-8}	3.2613×10^{-8}
12	26.40	1273.60	1.8869×10^{-8}	5.9577×10^{-8}
13	47.77	1273.61	2.9740×10^{-8}	1.3883×10^{-7}

climb dominates for high temperature and high stresses. Nabarro-Herring creep makes only a small contribution at temperatures near the melting point.

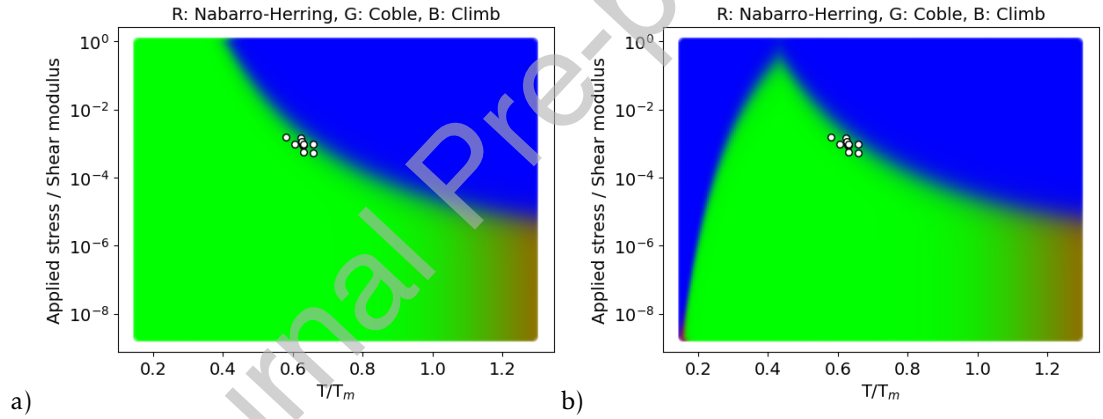

Figure 9: An Ashby diagram illustrating the relative contribution of Nabarro-Herring (red), Coble (green), and climb (blue) creep at a given stress and temperature, for a) $\dot{F} = 0$ $m^{-3}s^{-1}$ and b) $\dot{F} = 10^{19}$ $m^{-3}s^{-1}$. The white data points indicate the conditions at which literature experiments had been carried out [49].

The conditions at which the experimental data from Ref. [49] were measured are shown by white data points in Fig. 9. Table 6 shows the same conditions alongside the measured creep rates and the values predicted by our model (assuming a grain size of 20 μm). All of our model predictions are within one order of magnitude of the experimental data, with an average error of ±38%. Given the exponential nature of an Arrhenius relationship and that no experimental data was used to derive our model, this represents reasonable agreement. Additionally, there is a degree of uncertainty within the experiments that prevents perfect agreement.

Figure 10 is a parity plot comparing the model predictions (y-axis) with the experimental data

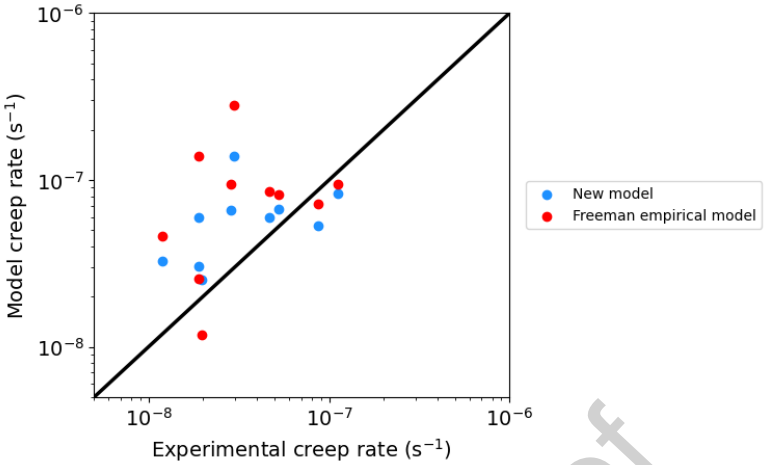

Figure 10: A parity plot comparing the modeled creep rate against the results from compressive creep tests [49]. The new model presented here is shown alongside the empirical model from Freeman [24]. The solid line indicates perfect agreement between the experiment and the model.

(x-axis). The results using the new model presented in this report are shown in blue alongside the empirical model developed by Freeman [24] in red. The closer the points are to the solid black line the better the agreement between experiment and modeling. Our model predicts slightly lower creep than the empirical correlation of Freeman et al. [24]. Figure 10 shows that application of the DFT and cluster dynamics data for point defect diffusivity provides a slight improvement on the empirical Freeman model [24, 50] that was derived from a subset of the experimental data shown in Table 6. The agreement between our model and the experimental data is worse for the highest temperature data (at 1273 K). Although for most of the temperatures examined experimentally the Coble creep mechanism is dominant in our model, the climb-limited mechanism becomes more influential at these higher temperatures. As discussed in the previous section, we have assumed the simplest relationship for this mechanism with an exponent of 3, whereas in reality processes, such as pipe diffusion, can lead to exponents in excess of 3. Future work should improve the description of climb-limited creep to move beyond the simple third order relationship assumed here. Additionally, the new model has the benefit of including the dependence of creep rate on grain size and fission rate density, which enables coupling to a grain growth model for U_3Si_2 or to variations in the linear heating rate, respectively. Note that the impact of varying grain size on irradiation-enhanced diffusivity (through their role as sinks), which would in turn influence the creep rate beyond the correlation shown in Eqs. (23) and (29), has not been included. More broadly, there is additional built-in uncertainty regarding the decision to use the same sink and source strength as for UO_2, as discussed in Section 3.1.1 in relation to the parametric study shown in Fig. 4.. However, given that the irradiation-enhanced creep rates are so low in our model, this will not influence the in-reactor behavior of U_3Si_2. We also note that validation of our model would benefit from additional experimental data than spans a larger range of conditions.

3.4. Implementation of creep model in BISON

The description of creep in U_3Si_2, given by the sum of the Nabarro-Herring (see Eq. (28)), Coble (see Eq. (34)), and climb (see Eq. (36)) contributions, has been implemented into the BISON fuel performance code to demonstrate the application of the lower length scale (LLS) informed creep model for engineering scale simulations.

Due to the very high thermal conductivity of U_3Si_2 [3] the temperatures are low, compared to UO_2, for typical LWR operating conditions (e.g., linear powers of 20-25 kW/m). Furthermore, the irradiation-enhanced terms (proportional to $\dot{F}$) are also very small. As such, for normal LWR linear powers virtually no creep is observed. Therefore, in order to test the model for higher temperatures a steady-state linear power of 35 kW/m, which might occur in a test reactor, was also examined and held for ~3.2 years. Figure 11 presents a) the predicted fuel outer diameter at the end of the simulation as well as b) the time history of the fuel centerline temperature during the simulation. One observes that the end-of-life diameter is slightly larger (< 0.01 mm) in the case with creep indicating that by computing creep there is an observable, but insignificant effect on the final fuel diameter. Similarly, the larger fuel diameter results in a marginally lower average centerline temperature due to a reduced pellet-clad gap, which increases the gap conductance. The jaggedness at the pellet ends are associated with pellet hourglassing, however, this effect is minimal due to the total scale of the abscissa in Fig. 11a is on the order of 10s of microns.

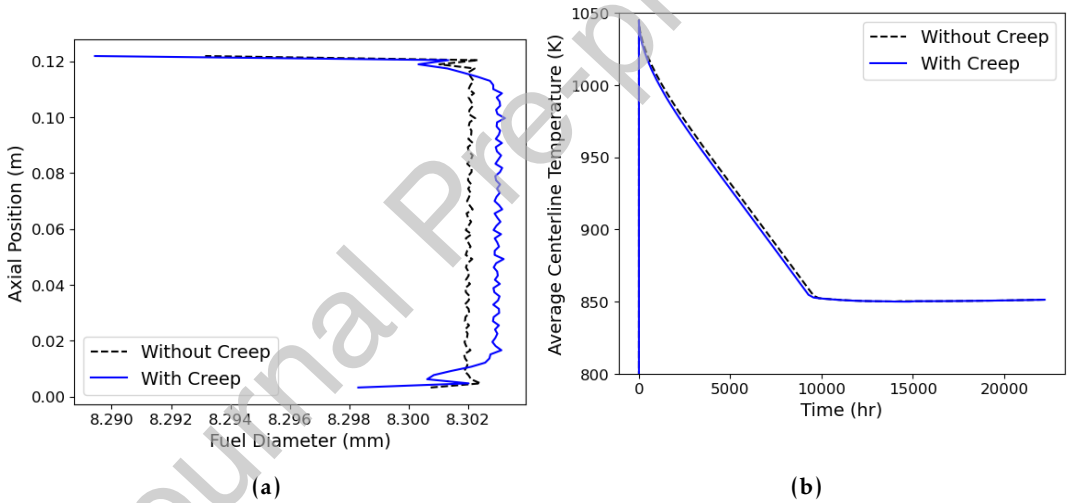

Figure 11: The (a) end-of-life diameter of the fuel and (b) the time history of the average centerline temperature.

To examine the possibility that a temperature transient due to a LOCA might cause higher creep rates, an increasing temperature on the outer cladding surface was prescribed, as shown in Fig. 12. This temperature corresponds to the maximum prescribed temperature and a sinusoidal profile is applied such that the temperature is 20 K less at the rodlet ends. Figure 13 shows the distribution of the creep strain (radial, axial, and hoop directions) throughout the pellet at the end of the LOCA simulation. It can be seen that the strain is still limited, despite the higher temperature induced by the LOCA. This is due to the failure of the cladding at 1100 K, as a result

of ballooning. At such temperatures, the creep model derived in this work still results in low creep rates. Following the failure of the cladding, the temperature continues to increase up to 1400 K where significant creep rates might be expected. However, following failure of the cladding the stress imparted by the cladding and rod internal pressure on the pellets has been eliminated, thus, removing the driving force for creep. Under a station blackout scenario, whereby the pressure on the fuel remains as the temperatures rise, the creep of U_3Si_2 might become more significant for fuel performance.

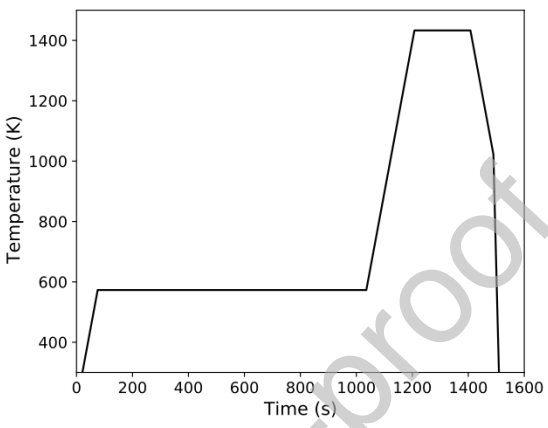

Figure 12: The cladding temperature prescribed during the LOCA transient.

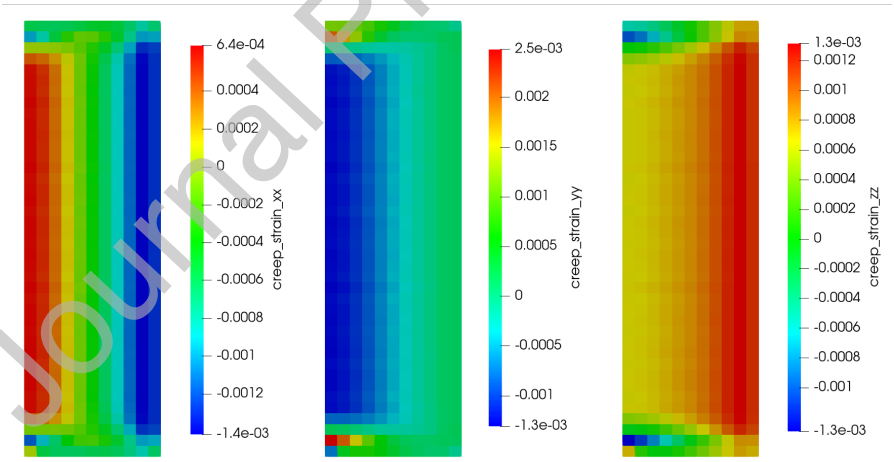

Figure 13: The distribution of the creep strain in (left) radial, (middle) axial, and (right) hoop directions throughout the pellet at the end of the LOCA simulation. Note the differences in scales.

4. Conclusions

U_3Si_2 is considered as an advanced nuclear fuel candidate due to its high thermal conductivity and high uranium density. These properties are beneficial for the performance and economics of nuclear fuel. However, due to the lack of experience using U_3Si_2 as a nuclear fuel there is limited data for the thermophysical and thermomechanical properties that are required to build fuel performance modeling capability. In this work, we employ atomic scale simulations of point defect self-diffusion under irradiation to derive a creep model for U_3Si_2.

Atomic scale modeling in combination with cluster dynamics simulations have been used to examine self-diffusion in U_3Si_2. It was found that thermal equilibrium diffusion (D_1) and athermal atomic mixing due to ballistic cascades (D_3) dominate self-diffusion, whereas irradiation-enhanced diffusion (D_2) did not contribute significantly. In addition to irradiation-enhanced bulk diffusion (described by D_1, D_2, and D_3), grain boundary diffusivity (in-plane), $D_{GB_{\|}}$, was simulated using MD, finding that U has higher $D_{GB_{\|}}$ than Si.

Based on the thermal equilibrium (D_1) and the irradiation-enhanced (D_2) defect concentrations and their mobilities in bulk U_3Si_2, models for Nabarro-Herring creep and dislocation climb were derived. Similarly, a Coble creep model was developed using the MD simulation results for grain boundary diffusion. The combined creep model captures the impact of fission rate, stress, and grain size on creep rate. The new creep model compared reasonably with the available experimental data and has been implemented in the fuel performance code BISON. The model was tested for both steady-state and LOCA conditions, finding that limited creep occurred. As more experimental data for U_3Si_2 creep becomes available the model should be further validate to confirm this finding.

Acknowledgments

Funding for this work was provided by the US Department of Energy, Office of Nuclear Energy NEAMS (Nuclear Energy Advanced Modeling and Simulation) and CASL (Consortium for Advanced Simulation of Light Water Reactors) programs. Los Alamos National Laboratory, an affirmative action/equal opportunity employer, is operated by Triad National Security, LLC, for the National Nuclear Security Administration of the U.S. Department of Energy under Contract No. 89233218CNA000001.

References

References

[1] S. L. Hayes, J. K. Thomas, and K. L. Peddicord. Material Property Correlations for Uranium Mononitride III. Transport properties. Journal of Nuclear Materials, 171:289–299, 1990.

[2] B. Szpunar, J. I. Ranasinghe, L. Malakkal, and J. A. Szpunar. First principles investigation of thermal transport of uranium mononitride . Journal of Physics and Chemistry of Solids, 146:109636, 2020.

[3] J. T. White, A. T. Nelson, J. T. Dunwoody, D. D. Byler, D. J. Safarik, and K. J. Mcclellan. Thermophysical properties of U_3Si_2 to 1773 K. Journal of Nuclear Materials, 464:275–280, 2015.

[4] P. A. Burr, E. Kardoulaki, R. Holmes, and S. C. Middleburgh. Defect evolution in burnable absorber candidate material: Uranium diboride, UB_2. Journal of Nuclear Materials, 513:45–55, 2019.

[5] E. Kardoulaki, J. T. White, D. D. Byler, D. M. Frazer, A. P. Shivprasad, T. A. Saleh, B. Gong, T. Yao, J. Lian, and K. J. Mcclellan. Thermophysical and mechanical property assessment of UB_2 and UB_4 sintered via spark plasma sintering. Journal of Alloys and Compounds, 818:153216, 2020.

[6] Y.-S. Kim. Uranium intermetallic fuels (U-Al, U-Si, U-Mo), in R Konings (Ed.), Comprehensive Nuclear Materials. 2012.

[7] J. Rest. A model for fission-gas-bubble behavior in amorphous uranium silicide compounds. Journal of Nuclear Materials, 325(2-3):107–117, 2004.

[8] T. C. Wiencek, R. F. Domagala, and H. R. Thresh. Thermal Compatibility Studies of Unirradiated Uranium Silicide Dispersed in Aluminum. Nuclear Technology, 71:608–616, 1985.

[9] M. Ross Finlay, G. L. Hofman, J. Rest, and J. L. Snelgrove. Behaviour of Irradiated Uranium Silicide Fuel Revisited. In International Meeting on Reduced Enrichment for Research and Test Reactors, 2002.

[10] J. Rest and G. L. Hofman. DART Model for Irradiation-Induced Swelling of Uranium Silicide Dispersion Fuel Elements. Nuclear Technology, 126(1):88–101, 1999.

[11] Y. S. Kim, G. L. Hofman, J. Rest, and A. B. Robinson. Temperature and dose dependence of fission-gas-bubble swelling in U3Si2. Journal of Nuclear Materials, 389(3):443–449, 2009.

[12] G. L. Hofman. Crystal Structure stability and fission gas swelling in intermetallic uranium compounds. Journal of Nuclear Materials, 140:256–263, 1986.

[13] R. C. Birtcher, J. W. Richardson, and M. H. Mueller. Amorphization of U3Si2 by ion or neutron irradiation. Journal of Nuclear Materials, 230:158–162, 1996.

[14] R. C. Birtcher, J. W. Richardson, and M. H. Mueller. Amorphization of U3Si by ion or neutron irradiation. Journal of Nuclear Materials, 244(3):251–257, 1997.

[15] M. R. Finlay, G. L. Hofman, and J. L. Snelgrove. Irradiation behaviour of uranium silicide compounds. Journal of Nuclear Materials, 325(2-3):118–128, 2004.

[16] M. A. Feraday, G. H. Chalder, and K. D. Cotnam. Irradiation Behavior of Cored U_3Si_2 Fuel Elements. Nuclear Applications, 4(3):148–153, 1968.

[17] I. J. Hastings, J. R. MacEwan, and L. R. Bourque. Effect of Swelling on Thermal Conductivity and Postirradiation Densification of U_3Si. Journal of the American Ceramic Society, 55:240–242, 1972.

[18] I. J. Hastings. Burnup and temperature dependence of swelling in U3Si. Journal of Nuclear Materialsr, 41:195–202, 1971.

[19] R. B. Matthews and M. L. Swanson. Swelling of Uranium Silicide Fuel During Postirradiation Heating. Nuclear Technology, 26(3):278–286, 1975.

[20] E. Sooby Wood, J. T. White, C. J. Grote, and A. T. Nelson. U_3Si_2 behavior in H_2O: Part I, flowing steam and the effect of hydrogen. Journal of Nuclear Materials, 501:404–412, 2018.

[21] A. T. Nelson, A. Migdisov, E. Sooby Wood, and C. J. Grote. U_3Si_2 behavior in H_2O environments: Part II, pressurized water with controlled redox chemistry. Journal of Nuclear Materials, 500:81–91, 2018.

[22] C. Herring. Diffusional Viscosity of a Polycrystalline Solid. Journal of Applied Physics, 21(437-445), 1950.

[23] R. L. Coble. A Model for Boundary Diffusion Controlled Creep in Polycrystalline Materials. Journal of Applied Physics, 34:1679, 1963.

[24] R. A. Freeman, T Martin, E Roberts, and T W Knight. Analysis of thermal creep for uranium silicide fuel using BISON. In Proceedings of the International Congress on Advances in Nuclear Power Plants - ICAPP 2018, 2018.

[25] D. A. Andersson, P. Garcia, X.-Y. Liu, G. Pastore, M. Tonks, P. Millett, B. Dorado, D. R. Gaston, D. Andrs, R. L. Williamson, R. C. Martineau, B.P. Uberuaga, and C.R. Stanek. Atomistic modeling of intrinsic and radiation-enhanced fission gas (Xe) diffusion in $UO_{2\pm x}$: Implications for nuclear fuel performance modeling. Journal of Nuclear Materials, 451(1-3):225–242, 2014.

[26] M. Tonks, D. A. Andersson, R. Devanathan, R. Dubourg, A. El-Azab, M. Freyss, F. Iglesias, K. Kulacsy, G. Pastore, S. R. Phillpot, and M. Welland. Unit mechanisms of fission gas release: Current understanding and future needs. Journal of Nuclear Materials, 504:300–317, 2018.

[27] R. Perriot, C. Matthews, M. W. D. Cooper, B. P. Uberuaga, C. R. Stanek, and D. A. Andersson. Atomistic modeling of out-of-pile xenon diffusion by vacancy clusters in UO_2. Journal of Nuclear Materials, 520:96–109, 2019.

[28] C. Matthews, R. Perriot, M. W. D. Cooper, C. R. Stanek, and David A Andersson. Cluster dynamics simulation of uranium self-diffusion during irradiation in UO_2. Journal of Nuclear Materials, 527:151787, 2019.

[29] C. Matthews, R. Perriot, M.W.D. Cooper, C. R. Stanek, and D. A. Andersson. Cluster Dynamics Simulation of Xenon Diffusion During Irradiation in UO_2. Journal of Nuclear Materials, In Progres, 2019.

[30] G. Martin, S. Maillard, L. Van Brutzel, P. Garcia, B. Dorado, and C. Valot. A molecular dynamics study of radiation induced diffusion in uranium dioxide. Journal of Nuclear Materials, 385(2):351–357, 2009.

[31] J. L. Wormald and A. I. Hawari. Examination of the impact of electron-phonon coupling on fission enhanced diffusion in uranium dioxide using classical molecular dynamics. Journal of Materials Research, 30(9):1485–1494, 2015.

[32] M. W. D. Cooper, C. R. Stanek, J. A. Turnbull, B. P. Uberuaga, and D. A. Andersson. Simulation of radiation driven fission gas diffusion in UO_2, ThO_2 and PuO_2. Journal of Nuclear Materials, 481:125–133, 2016.

[33] D. A. Andersson, X-Y. Liu, B. Beeler, S. C. Middleburgh, A. Claisse, and C. R. Stanek. Density functional theory calculations of self- and Xe diffusion in U_3Si_2. Journal of Nuclear Materials, 515:312–325, 2019.

[34] B. Beeler, M. I. Baskes, D. A. Andersson, M. W. D. Cooper, and Y. Zhang. A modified Embedded-Atom Method interatomic potential for uranium-silicide. Journal of Nuclear Materials, 495:267–276, 2017.

[35] F. A. Kröger and H. J. Vink. Relations between the concentrations of imperfections in crystalline solids. J. Solid State Phys., 3:307–435, 1956.

[36] S. Plimpton. Fast Parallel Algorithms for Short – Range Molecular Dynamics. Journal of Computational Physics, 117:1–19, 1995.

[37] A. P. Moore, B. Beeler, C. Deo, M. I. Baskes, and M. A. Okuniewski. Atomistic modeling of high temperature uranium-zirconium alloy structure and thermodynamics. Journal of Nuclear Materials, 467:802–819, 2015.

[38] J. Ziegler, J. Biersack, and U. Littmark. Stopping and Ranges of Ions in Matter,. Pergamon Press, 1985.

[39] B. Beeler, M. Baskes, D. A. Andersson, M. W. D. Cooper, and Y. Zhang. Molecular dynamics investigation of grain boundaries and surfaces in U_3Si_2. Journal of Nuclear Materials, 514:290–298, 2019.

[40] M. Helin and J. Flygare. NRC LOCA tests at Studsvik: Design and construction of test train device and test with unirradiated cladding material. Technical Report STUDSVIK/N-11/130, 2012.

[41] M. Flanagan and P. Askeljung. Observations of Fuel Fragmentation, Mobility and Release in Integral, High-Burnup, Fueled LOCA Tests. Presented at the LOCA workshop of the May 2012 Halden Program Group Meeting in Lyon, France.

[42] H. Shimizu. The properties and irradiation behavior of U_3Si_2. Technical Report NAA-SR-10621, Atomics International, 1965

[43] B. Beeler, M. W. D. Cooper, Z.-G. Mei, D. Schwen, and Y. Zhang. Radiation driven diffusion in γU-Mo. Journal of Nuclear Materials, 543:152568, 2021.

[44] C. Matthews, D. Schwen, and A. C. Klein. Radiation re-solution of fission gas in non-oxide nuclear fuel. Journal of Nuclear Materials, 457:273–278, 2015.

[45] Hj. Matzke. Diffusion processes and surface effects in non-stoichiometry nuclear fuel oxides UO_{2+x} and (U, Pu)$O_{2\pm x}$. J. Nucl. Mater., 114:121–135, 1983.

[46] F. R. N. Nabarro. Deformation of Crystals by the Motion of Single Lonsin Report of a Conference on the Strength of Solids (Bristol, U.K.). Physical Society London, pages 75–90, 1948.

[47] C. Herring. Diffusional Viscosity of a Polycrystalline Solid. Journal of App, 21:437, 1950.

[48] J. P. Hirth and J. Lothe. Theory of Dislocations. 1968.

[49] T. W. Knight. U_3Si_2 Fabrication and Testing for Implementation into the BISON Fuel Performance Code. US DOE Technical report, 2018, DOI: doi.org/10.2172/1434631.

[50] K A Gamble, G. Pastore, M.W.D. Cooper, and David A Andersson. AFT material model development and validation for priority fuel concepts, CASL Tech. rep. L3:FMC.FUEL.P19.06. Technical report, 2019.

M. W. D. Cooper: Conceptualization, Methodology, Investigation, Visualization, Writing - Original Draft.

K. A. Gamble: Conceptualization, Software, Methodology, Visualization, Investigation, Writing - Original Draft.

L. Capolungo: Conceptualization, Methodology, Writing - Review & Editing.

C. Matthews: Methodology, Software, Writing - Review & Editing.

D. A. Andersson: Conceptualization, Supervision, Methodology, Writing - Review & Editing.

B. Beeler: Methodology, Writing - Review & Editing.

C. R. Stanek: Supervision, Writing - Review & Editing.

K. Metzger: Conceptualization, Methodology, Writing - Review & Editing

Declaration of interests

The authors declare that they have no known competing financial interests or personal relationships that could have appeared to influence the work reported in this paper.